Heterogeneous & Homogeneous & Bio- & Nano-
CHEMCATCHEM
CATALYSIS

Accepted Article

Title: Nickel exsolution-driven phase transformation from an n = 2 to an n= 1 Ruddlesden-Popper manganite for methane steam reforming reaction in SOFC conditions

Authors: Sebastián Vecino-Mantilla, Paola Gauthier-Maradei, Marielle Huvé, José Manuel Serra, Pascal Roussel, and Gilles H. Gauthier

To be cited as: *ChemCatChem* 10.1002/cctc.201901002

Link to VoR: http://dx.doi.org/10.1002/cctc.201901002

A Journal of
ChemPubSoc Europe

WILEY-VCH

www.chemcatchem.org

10.1002/cctc.201901002

WILEY-VCH

FULL PAPER

Nickel exsolution-driven phase transformation from an n = 2 to an n= 1 Ruddlesden-Popper manganite for methane steam reforming reaction in SOFC conditions

Sebastián Vecino-Mantilla[a][b], Paola Gauthier-Maradei[a], Marielle Huvé[c], José Manuel Serra[b], Pascal Roussel[c], Gilles H. Gauthier*[a]

Abstract: An original way to perform the exsolution of Ni nanoparticles on a ceramic support was explored for the development of methane steam reforming catalyst in SOFC anode conditions. The n=2 Ruddlesden-Popper (RP) phase $La_{1.5}Sr_{1.5}Mn_{1.5}Ni_{0.5}O_7$ has been synthesized by the Pechini method and subsequently reduced with an H_2-N_2 mixture at different temperatures and reduction times to induce the formation of two phases: $LaSrMnO_4$ (n=1 RP) decorated with metallic Ni nanoparticles. Preliminary measurements of catalytic behavior for the steam reforming have been carried out in a reduction-reaction process with a mixture of 82 mol%CH_4, 18 mol%N_2 and low steam to carbon ratio (S/C=0.15). The catalyst exhibits a selectivity for CO production (0.97), 14.60 mol% CH_4 conversion and around 24.19 mol% H_2 production. Such catalytic behavior was maintained for more than 4 h, with a constant rate of hydrogen production and CH_4 conversion rate.

Introduction

Given the current environmental problems and the global energetic context, it is necessary to develop and implement new, clean, safe and reliable energetic alternatives, which ensure a high and sustainable quality of life and, at the same time, avoid a possible crisis. Presently, the Solid Oxide Fuel Cells (SOFCs) are studied as potential devices to produce electricity and heat in a clean and efficient way (chemical to electrical yield > 60 %), better than conventional thermomechanical processes, converting directly the chemical energy of an oxidant gas and a large range of fuels (fuel flexibility), without combustion as intermediate step.[1,2] Nevertheless, the massive commercialization of SOFCs is blocked mainly by cost and durability issues, such as stability at high temperature (600 – 1000 °C), compatibility with the other components of the cell, electrochemical activity at low temperature and direct operation with hydrocarbon fuels without coking or poisoning (catalytic behavior).[3,4] In particular, the conventional cermet based on nickel and yttria-stabilized zirconia (Ni/YSZ) still presents many issues as SOFC anode material.[5,6] Therefore, one of the current interests in this field is the search for new materials that can solve these problems in the cells and allow its proper operation.

One of the most promising alternatives is the development of Mixed Ionic and Electronic Conducting (MIEC) anodes. Apart from the perovskite mixed oxides, the Ruddlesden-Popper (RP) phases have demonstrated such kind of behavior, and generated great expectation, historically as SOFC cathodes.[7,8] Due to their varied and exceptional transport and structural properties, together with their high thermal and mechanical stabilities, those materials are considered as an interesting option in a variety of catalytic and electrocatalytic processes like those occurring at both electrodes of an SOFC.[9–18]

RP phases are materials whose structure results from the intergrowth of one or several perovskite-type blocks (ABO_3) separated by one rock-salt structure layer (AO). Their general formula is $A_{n+1}B_nO_{3n+1}$ or $(AO)(ABO_3)_n$, where A represents alkali, alkaline earth, or rare earth metal cations located in the perovskite and rock salt slabs, B refers to transition metal cations occupying the anionic octahedral coordination of the perovskite block, and n is the number of octahedra's layers in the perovskite block.[19] Their possible use as anode material has been only recently described and studied[20,21] and the resulting manganite family could be a viable option. Several compositions have shown an exceptional potential as an electrode (both anode and cathode) in symmetrical SOFCs due to their stability in oxidizing and reducing atmospheres, thermo-mechanical compatibility with common electrolytes *e.g.* gadolinium-doped ceria (CGO), and acceptable electrochemical properties, high temperature resistance, redox stability and favorable total conductivity.[22,23] Notwithstanding, some authors suggest that some compositions, *e.g.* $La_{0.6}Sr_{1.4}MnO_4$, are poor catalysts for direct use of methane.[24]

[a] S. Vecino-Mantilla, Dr. G. Gauthier, Dr. P. Gauthier-Maradei
Grupo de investigación INTERFASE, escuela de ingeniería química, Universidad Industrial de Santander, carrera 27 calle 9, ciudad universitaria, Bucaramanga, Colombia
E-mail: gilgau@uis.edu.co
[b] S. Vecino-Mantilla, Dr. J.M. Serra
Instituto de Tecnología Química (Universitat Politècnica de València – Consejo Superior de Investigaciones Científicas), Avd. de los Naranjos s/n, 46022 Valencia, Spain.
[c] M. Huvé, Dr. P. Roussel
Université de Lille, CNRS, Centrale Lille, ENSCL, Université d´Artois, UMR 8181 - UCCS - Unité de Catalyse et Chimie du Solide, F-59000 Lille, France

Supporting information for this article is given via a link at the end of the document.

It is however well known that electrochemical characteristics and catalytic behavior of a mixed oxide anode can be improved by the addition of small metallic nanoparticles (Ni, Ru, Rh, others) on the surface of the MIEC using, for example, the impregnation technique. Nevertheless, the use of impregnated material followed by a heat-treatment at high temperature (> 700 °C) does not guarantee a homogeneous distribution, size and a strong metal-support interaction (nanoparticles anchorage)[25,26] to avoid sintering problems *in operando*. As an alternative method to create heterogeneous surface systems, it is possible to dissolve active metals in their oxidized form within the electrode material phase during the synthesis step. Then, under reducing atmosphere and high temperature (driven force), nanosized metallic particles can precipitate from the bulk to the surface. This phenomenon is called *in situ* growth or exsolution[8,25,27–29] and, as is previously presented, it could be considered as the basis for the design and development of more sophisticated oxide materials with advanced functionality.[30] Even though, such mechanism has been applied mainly for perovskite structural oxides[31–34] and until now few examples of exsolution in RP compounds have been reported[27,29]

This study describes the preparation of a new RP material, $La_{1.5}Sr_{1.5}Mn_{1.5}Ni_{0.5}O_7$ (LSMN n= 2), which has been designed using a retrosynthetic approach similar to organic chemistry,[35,36] in order to be able to form, in reducing conditions, a biphasic material made of electrocatalytic active metallic nanoparticles on a n= 1 RP manganite of the type $La_xSr_{2-x}MnO_4$. The synthesis, proof of exsolution and its catalytic behavior for the methane steam reforming reaction using Colombian natural gas composition in low water content is presented.

Results and Discussion

LSMN n= 2 study

The LSMN n= 2 material exhibits a Ruddlesden-Popper (RP) structure with 2 layers of octahedra in the perovskite-like stack and tetragonal space group *I4/mmm* (No. 139). A total of 24 sets of ~3 g of corresponding material, were synthesized as described in the Experimental Section. For each synthesis, the lattice parameters (*a*=*b*, *c*) and the unit-cell volume were determined from the XRD data using structure refinement based on the Full Pattern Matching – Le Bail method. The comparison of the results allowed the selection of the samples to be mixed (or discarded), obtaining a final homogeneous stock of around 40 g of pure phase material (see Supplementary Information; Figure S1 and Table S1).

The structure of the as-obtained LSMN n= 2 powder was successfully refined as a single phase using Rietveld method based on X-ray diffraction data and pseudo-Voigt peak shape function with reasonable reliability factors of R_p= 4.35 %, R_{wp}= 5.77 %, and χ^2= 1.51 and very few residual intensity, as observed graphically in Figure 1, suggesting an effective structural analysis. The refined lattice parameters are shown in Table 1 and those results agree well with those reported for parent compounds such as $La_{1.4}Sr_{1.6}Mn_2O_7$ obtained at 1450 °C,[37] $LaSr_2Mn_{1.6}Ni_{0.4}O_7$ prepared at 1500 °C[38] and, to a greater extent, $La_{1.5}Sr_{1.5}Mn_{1.25}Ni_{0.75}O_{6.67}$[39] synthesized at a higher temperature (1450 ºC). In fact, the small differences are especially associated with the stoichiometric La/Sr and/or Mn/Ni ratio, the synthesis method, or the sintering temperature. As often the case of transition metal oxides, the substitution at the A or B-sites of the structure is correlated with a mechanism of charges compensation, which implies changes in the unit cell size. Finally, this material was analyzed by X-ray fluorescence (XRF) with a result of 0.057 ± 0.002 weight fraction, confirming the adequate stoichiometric Ni amount in the solid-state solution (see Supplementary Information; Figure S2).

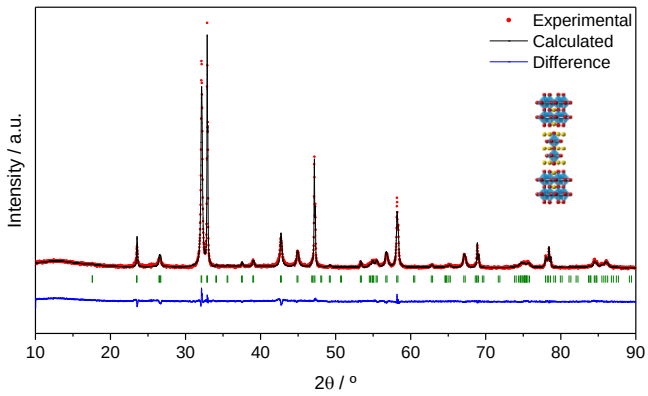

Figure 1. LSMN n= 2 Rietveld refinement.

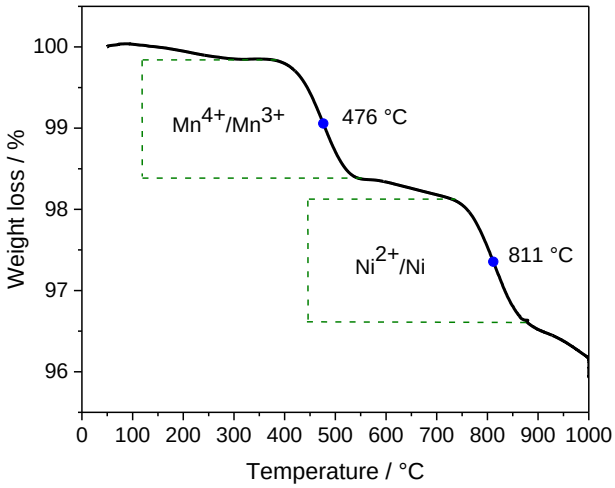

Figure 2. LSMN n= 2 thermogravimetric analysis in reducing atmosphere.

Thermogravimetric analysis (TGA) performed from RT until 1000 °C in diluted H_2 is presented in Figure 2. Between room temperature and aprox. 850 °C, two weight losses are evidenced in distinct temperature range, that must be attributed to the reduction of Mn and/or Ni. In similar compositions of perovskite structure type, stabilized in addition by Cr at the B site, Ni^{2+} and mixed $Mn^{3+/4+}$ oxidation states have been clearly established.[40] We assume the same kind of defect equilibrium is also present in

10.1002/cctc.201901002

the LSMN n=2 material. Indeed, the first weight loss is observed between around 400 and 600 °C; this is the same temperature range for which Mn^{4+} is reduced to exactly Mn^{3+} in the $(La,Sr)_2MnO_{4+\delta}$ series synthesized in air and treated in the same conditions as the present work. [22] As a consequence, the first weight loss can be assigned to the reduction of Mn^{4+} to Mn^{3+}, with consecutive formation of oxygen vacancies, in agreement with the material charge balance. The second weight loss in reducing atmosphere is observed between 750 and 850 °C and is associated to the reduction of Ni^{2+} to Ni^0. Such attribution is based on the fact that the reduction of Mn^{3+} to Mn^{2+} in $(La,Sr)_2MnO_{4+\delta}$ parent compounds has been observed only for temperatures higher than 900 °C in similar conditions. [22] Indeed, this second weight loss measured between 730 and 860 °C corresponds to $\Delta m/m$=-1.43%. This is in very close agreement with the theoretical weight loss ($\Delta m/m$=-1.42%) calculated from the following equation, considering a fixed 3+ oxidation state for Mn [Eq. (1)]:

$$La_{1.5}Sr_{1.5}Mn_{1.5}Ni^{2+}_{0.5}O_{6.5} + H_2 \rightarrow 1.5\,LaSrMnO_4 + 0.5\,Ni + H_2O \quad (1)$$

It is worth noting that the reduction to metal of Ni cations only is confirmed by thermodynamic calculations for the reduction of binary metal oxides of corresponding constituting elements (see details in Supplementary Information; Figure S3).

Table 1. LSMN n= 2 structure parameters calculated by Rietveld refinement using XRD data

$La_{1.5}Sr_{1.5}Mn_{1.5}Ni_{0.5}O_{7\pm\delta}$ (LSMN n= 2)			
	This study		
R_p [%]	3.80		
R_{wp}[%]	4.92		
χ^2	1.29		
a [Å]	3.8546(2)		
c [Å]	20.1911(14)		
V [Å^3]	300.01(3)		
	$La_{1.4}Sr_{1.6}Mn_2O_7$ [37]	$LaSr_2Mn_{1.6}Ni_{0.4}O_7$ [38]	$La_{1.5}Sr_{1.5}Mn_{1.25}Ni_{0.75}O_{6.67}$ [39]
R_p	9.53	[N.R.]	10.6
R_{wp}	12.36	[N.R.]	12.9
χ^2	1.4	[N.R.]	[N.R.]
a [Å]	3.8686(6)	3.8502(1)	3.847(2)
c [Å]	20.238(4)	20.1134(6)	20.137(1)
V [Å^3]	302.88(3)	298.17(2)	298.02

[N.R.]: Not-reported

As expected, metal oxides such as La_2O_3, SrO and MnO show positive Gibbs free energy (ΔG) in the selected temperature range; consequently, and in agreement with chemical knowledge of the corresponding elements, these oxides are very difficult to reduce using H_2. On the other hand, the three other manganese oxides *i.e.* Mn_3O_4, Mn_2O_3 and MnO_2, as well as NiO shall be the only easily reducible oxides, because of their calculated negative ΔG, what is in concordance with the thermogravimetric analysis.[6,41–43] If such weight loss assignment is correct, Ni exsolution should be evidenced for temperature treatment in reducing conditions between T=750 °C and T=850 °C. According to these results, the operating temperatures (T) for reduction (and subsequent catalytic tests) were selected as T= 750, 800 and 850 °C, together with the following reduction times: t_r= 1, 4, 8, 16, 24 and 48 h, as described in the Experimental Section.

Exsolution study

The XRD patterns of LSMN n= 2 after reduction at 750 °C in 3 mol% H_2/N_2 are shown in Figure 3 as a function of the reduction time t_r. By heating LSMN n= 2 oxide in reducing atmosphere at 750 °C and short reduction times, a mixture of phases is obtained. During the first hour the LSMN n= 2 phase changes and, although it is still visible in a large proportion, the formation of a new phase in a smaller quantity is also observed. At 4 h of reduction, it is evident that ratio is slowly reversed, decreasing the amount of the RP n= 2 phase. However, after 8 h of treatment, the sample exhibits two well-defined phases, completely different than the starting one, which can be indexed as a reduced Ruddlesden-Popper phase of the $LaSrMnO_4$ type (hereafter referred to as LSM n= 1) and metallic Ni (the characteristic peaks of Ni phase at around 44.5 and 51.9°, as shown as red dots in Figure 3).[44]

The formation of LSM n= 1 seems reasonable since the synthesis conditions of $La_xSr_{2-x}MnO_4$ (x ≥ 1) materials have been reported under reducing conditions.[45–47] Thus, the reduction products can be proposed according to the Eq. (1).

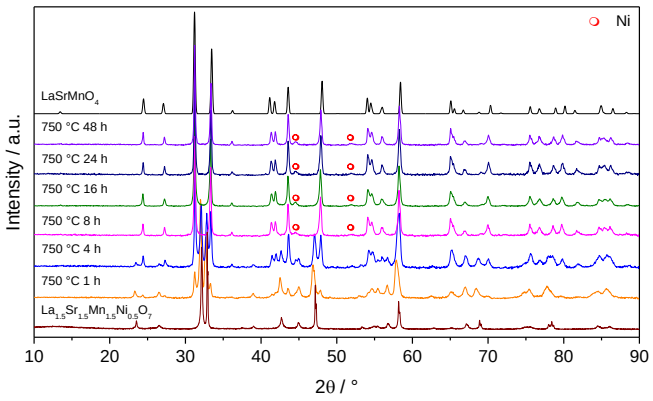

Figure 3. XRD patterns of LSMN n= 2 reduced at 750 °C during different times (t_r)

The reduced samples in which the two LSM n= 1 and Ni phases are clearly evidenced (t_r from 8 to 48 h at 750 °C) are apparently identical, indicating the process and material stability upon reduction. A complete quantitative Rietveld refinement using XRD data was carried out considering a K_2NiF_4-type structure with a tetragonal unit cell and *I4/mmm* space group for the LSM n= 1 structure and FCC cubic cell with *Fm-3m* space group for Ni. The results of lattice parameters of both phases and their weight fraction are shown in Figure 4 (A–E). The refinements present correct reliability factors, R_p= 4.26-5.12 %, R_{wp}= 5.34-6.67 % and "goodness of fit (GOF)" or χ^2= 1.28-1.93 (value between 1.0 and 2.9 is generally considered satisfactory),[48] confirmed by the

10.1002/cctc.201901002

graphical analysis of each refinement. Very slight evolution of the lattice parameters can be evidenced along with the reduction duration with an apparent *a* decrease while *c* parameter increases for the LSM n= 1 up to t_r= 24 h. The phenomenon seems to stabilize for larger reduction times. Nonetheless, neither the refined Ni lattice parameter nor the Ni weight fraction exhibits any change along with the reduction duration, what means the cell parameter changes for the n= 1 Ruddlesden-Popper phase is possibly related to the presence of defects formed during Ni exsolution that disappear within the crystal structure or the further slow reduction of the same manganite with time. It is worth nothing that for t_r= 24 h the refined values for the LSM n= 1 lattice parameters are in a good correspondence with the calculated for the same material synthesized by other authors.[49–52]

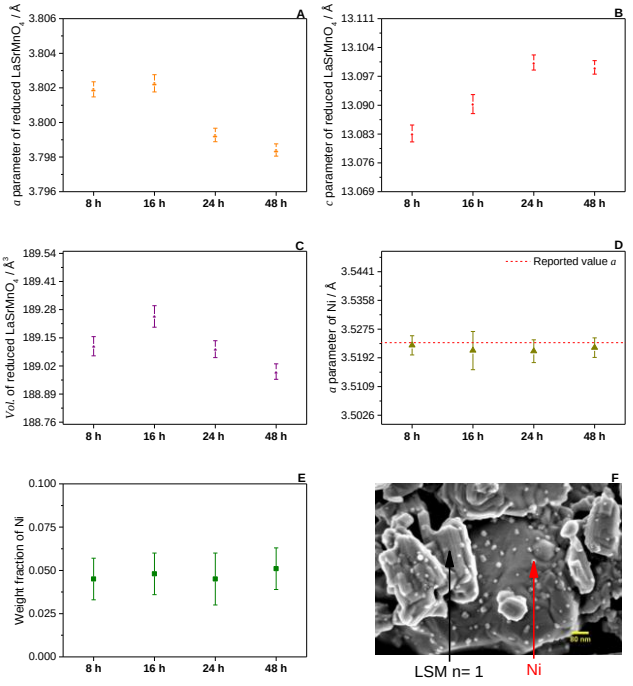

Figure 4. XRD Rietveld refinement of LSMN n= 2 reduced at 750 °C during 8, 16, 24 and 48 h. A) *a* parameter of reduced $LaSrMnO_4$. B) *c* parameter of reduced $LaSrMnO_4$. C) *Vol.* of reduced $LaSrMnO_4$ D) *a* parameter of Ni compared with the reported one E) Weight fraction of Ni F) SEM image of LSMN n= 2 reduced at 750 °C and 4 h.

The refined *a* lattice parameter calculated for metallic nickel in all four studied points match very well with the reported values (a= 3.5236(3) Å),[53] confirming that exsolved nanoparticles are probably pure Ni, what makes sense on a chemical point of view. In addition, the refined weight fraction of 0.050 for metallic Ni, identical for all studied points at the precision level of the refinement (at 3 times the standard deviation), is in a very good agreement with the maximum stoichiometric and theoretical values calculated using the above-mentioned Eq. (2) (0.946 LSM n= 1 and 0.054 Ni) as well in accordance with the amount of metallic Ni in LSMN n= 2, *i.e.* suggesting that all Ni^{2+} was completely reduced and exsolved from the crystal structure and visible as hemispherical nanoparticles on the surface of the manganite (Figure 4 F).

The XRD patterns of LSMN n= 2 after reduction in 3 mol% H_2/N_2 at 800 and 850 °C using the same values of t_r are shown in Supplementary Figures S4 and S5, respectively. In these cases, the intermediate mixture of phases is only visible for 1 h of reduction and, for t_r= 4 h, the LSM n= 1 and Ni phases are already formed with an increasing crystallinity when T and/or t_r raises. This result can be associated to faster kinetics of exsolution at higher temperature due to the fact that such kind of process requires solid state diffusion within the crystal framework.[54]

The same conclusions can be obtained as in the previous case (T= 750 °C), *i.e.* two phases are observed for reduction times between 4 and 48 h, which are almost identical along the series, except the slight change in the lattice parameters for the LSM n= 1 phase, already described in the low temperature exsolution conditions. For all reduction times, no difference can be evidenced for metallic Ni lattice parameter and weight fraction, as shown in Supplementary Figures S6 (A–E) and S7 (A–E), suggesting the complete Ni reduction and exsolution from the crystal structure and LSM n= 1 formation, as can be also confirmed in SEM results (Figure S6 F and Figure S7 F). Globally, in any reducing conditions (t ≥ 4 h), all the lattice parameters (*a*, *c* and cell volume) for LSM n= 1 phase, calculated by Rietveld refinement, remain coherent with the values reported by other authors;[49–52,55–59] the same can be concluded for Ni *a* lattice parameter and weight fraction.

TEM and STEM images of the exsolved nanoparticles and its perovskite matrix associated to energy dispersive spectroscopy (EDS) mapping of the main elements for a characteristic zone of LSMN n= 2 powder after reduction at 850 ºC for 4 h are shown in Figure 5. The elemental mapping (Figure 5 C) confirm the grain composition, *i.e.* La, Sr, and Mn are homogeneously distributed in the entire grain and few tenths of nanometer-sized highly concentered spots (in red) confirm the chemical nature of the nanoparticles, which consists in pure and dense metallic Ni. Only trace of Ni is detected in the area without Ni segregation, which suggest that most of the Ni is exsolved on the surface. The complete morphology of the reduced sample can be observed in Figure 5 D: the LSM n= 1 surface is decorated with some anchored small and uniformly distributed crystallized Ni hemispherical nanoparticles with strong particle - oxide matrix interaction.[54,60,61] The spacing between the lattice fringe are consistent with the (111) interreticular distance of Ni and the [001] zone axis of the perovskite. Such kind of morphological results (nanoparticles embedded on the surface) are similar and coherent with those reported for Ni exsolution from perovskites structures such as $La_{0.9}Mn_{0.8}Ni_{0.2}O_3$,[62] $La_{0.4}Sr_{0.4}Sc_{0.9}Ni_{0.1}O_3$[33] and $La_{0.5}Sr_{0.5}Ti_{0.75}Ni_{0.25}O_3$.[32]

If it has been established that the particle size distribution and average particle size values can be associated to many extrinsic (oxygen partial pressure P_{O_2} of the reduction gas mixture, etc) or

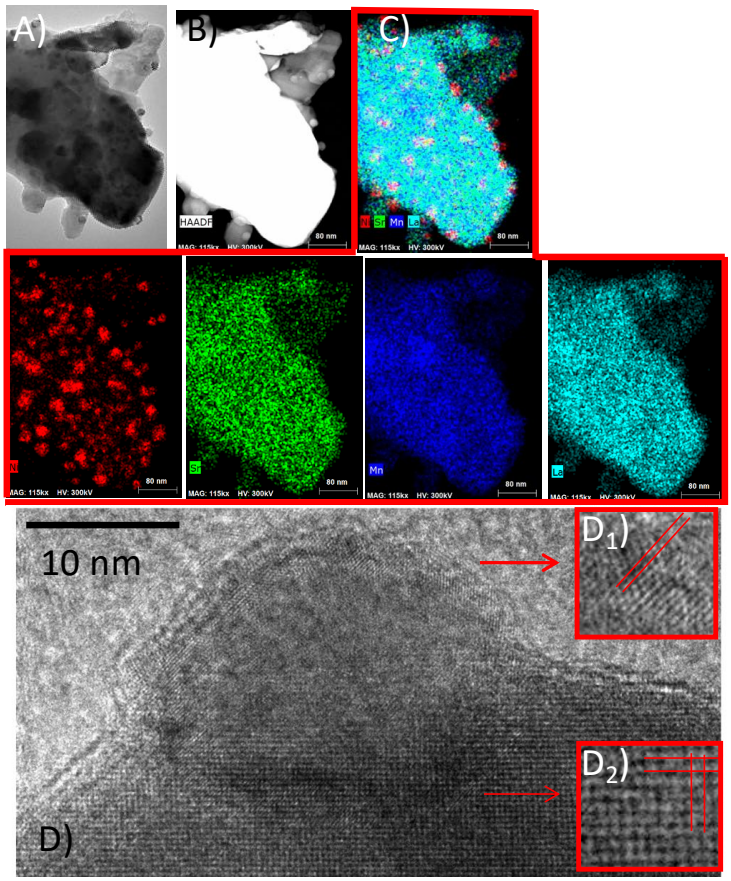

Figure 5. LSMN n= 2 powder reduced at 850 °C and 4 h A) TEM image B) HAADF images showing nanoparticles on the surface C) Corresponding EDS mapping identify them as Ni D) HR TEM image of the exsolved nanoparticle and its perovskite matrix. The lattice fringe spacings are D1) close to 2 Å which correspond to d_{111} of Ni and D2) close to 3.8 Å x 3.8 Å which match well with the [001] zone axis of a RP manganite.

intrinsic parameters (surface features,[63] mechanical stresses and strains,[64] wetting angles,[65] defects such as vacancies and dislocations[66,67]), affecting the formation (nucleation) and growth of the Ni particles,[33] it was considered in this study only the main effects of reduction temperature (T) and time (t_r).

The influence of T and t_r on the Ni particle size was examined using a precise image analysis of the scanning electron micrographs (FE-SEM) based on about 100 particles to obtain a characteristic frequency histogram in each selected (T, t_r) conditions. The grouped particle size data were analyzed using as likelihood fitting method a lognormal distribution [Eq. 2] as reported in the literature[68–70] and treated in OriginPro8® with the iteration algorithm named Orthogonal Distance Regression.

$$f(D)=\frac{A}{(2\pi)^{0.5}wD}e^{-\frac{\ln(D/D_0)^2}{2w^2}} \quad (2)$$

In this case, A is the area of the size distribution, w the scale parameter defining the width of the size distribution (multiplicative standard deviation) and D_0 the median diameter. The average particle size ($\bar{D}_p$) of the lognormal distribution and its standard deviation (σ_{ln}) were determined using the following equations:

$$\bar{D}_p=D_0e^{\frac{w^2}{2}} \quad (3)$$

$$\sigma_{ln}=D_0\sqrt{e^{2w^2}-e^{w^2}} \quad (4)$$

The results of the 14 lognormal distributions are shown in Supplementary Figure S8 and they were used to determine the statistical significance of the different studied variables (T and t_r) on the average Ni particle size ($\bar{D}_p$). A statistical ANOVA analysis was performed through the Generalized Linear Models available in the STATGRAPHICS Centurion XVII package with a confidence level of 95 % and a Square Sum Type III analysis, allowing the measurement of the contribution of each variable. The results are presented in Table 2, showing that p-value was lower than 0.05 for both cases, which means that t_r and T have a statistically significant influence on the average Ni particle size in perfect agreement with Gao *et al.*[33], Lai *et al.*[54] and Oh *et al.*[64]

The $\bar{D}_p$ results obtained from the distributions were used to generate the contour plot by a physical interpolating method (Thin Plate Spline, TPS). Figure 6 graphically shows the T and t_r effect

10.1002/cctc.201901002

on the average Ni particle size and confirms the results obtained with ANOVA (Table 2), in which both variables have a high influence on the particle size. Nevertheless, it is worth noting that the temperature effect is apparently stronger than the reduction time, *i.e.* high temperatures induce the rapid exsolution of Ni particles with a wide distribution. During the exsolution process, the self-grown nanoparticles are "anchored" and highly dispersed on the oxide surface, displaying a higher tendency to avoid their agglomeration and coarsening during the reduction/reaction steps; the resulting material consists in an excellent option to improve the catalytic behavior, prevent the sulfur poisoning and carbon formation when hydrocarbons are used as fuels.[71]

Table 2. Temperature and reduction time effect on $\bar{D}_p$ (ANOVA result)

Variable	Sum of squares	D.F.[*]	Mean square	F-test	p-value
Temperature (T)	724.435	1	724.435	34.36	0.0001
Reduction time (t_r)	520.277	1	520.277	24.67	0.0004
Residual	231.94	11	21.0855		
Total (Corrected)	1366.44	13			

[*] D.F.: Degree of freedom

The variation in the particle size and its slow increase with time at any studied reduction temperature could be associated with the fact that the metal exsolution equilibria has not been reached. Nevertheless, such hypothesis must be discarded, as it was already demonstrated with the complete Ni exsolution according to Eq. 1.

Therefore, two possible mechanisms are possible to explain the evolution of particles size due to sintering: particle migration followed by coalescence or Ostwald-ripening.[72] The first hypothesis is coalescence that only occurs between very close particles,[54,60,61] a process strongly T dependent[72–74] mainly when the Tamman temperature is exceeded ($0.5T_{melting}$ [K], Ni= 864 K).[75] When the nanoparticle-matrix oxide interaction is poor, the particle exhibits a spherical shape, generally observed *e.g.* using a typical metallic impregnation method. This case is more propitious to particle/crystallite migration and coalescence. However, it has been demonstrated that a strong interaction between the particles and the matrix turns the particle shape to hemispherical,[54,60,61] explained, in this case, by the fact that the exsolved phase is embedded into the oxide matrix.[64,71] Such characteristic makes them less mobile on the surface and the coalescence rate is considerably decreased, occurring only when the particles are very close to each other. This is the case of exsolved nanoparticles, as mentioned before and therefore cannot be the dominant mechanism.[54,76,77] As a consequence, the only mechanism that could explain the observed increase of nanoparticle size is probably Ostwald-ripening process. This mechanism describes the growth of a larger particle by consuming a smaller one without direct connection, here, clusters of atoms from a small particle migrate through the oxide surface and merge into another large particles just to reach the equilibrium; this effect becomes much serious when the temperature increases.[76,78] As indeed for the coalescence process, the driving force is the minimization of the total surface energy of the system.

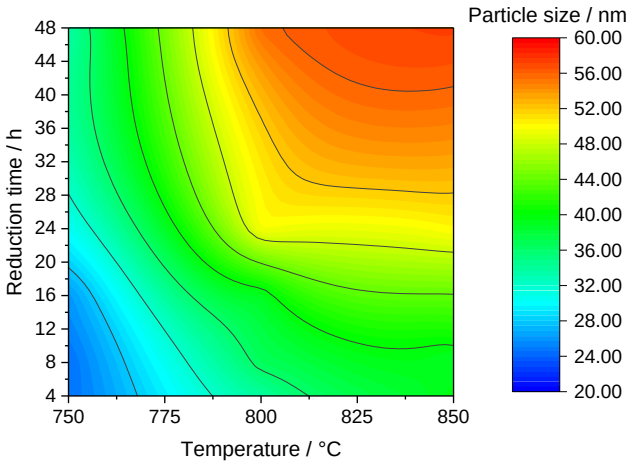

Figure 6. Influence of the reduction temperature (T) and time (t_r) on the Ni exsolved particle size.

Despite the possible presence of Ni particle sintering, the average particle size values and distributions obtained in the present study are similar (< 100 nm) to what has been described by other authors using exsolution of Ni or other metallic elements from an oxide matrix.[5,33,54,67,71,79,80]

Preliminary catalytic study

Preliminary catalytic properties of the material were studied in only one selected operating condition for exsolution *e.g.:* T= 850 °C and t_r= 16 h. The reaction was performed at the same temperature as for the reduction, T= 850 °C, using only small amount of water for the methane reforming, *i.e.* a low steam to carbon ratio (S/C) (GIR concept).[81] According to the literature, S/C ratios higher than 1 are necessary to avoid the coke formation/deposition on the anode surface. Nevertheless, such high S/C ratios dilute the fuel content and may lead to thermomechanical damages due to large temperature gradients in the anode side (reforming reaction strongly endothermic, while electrochemical reactions are exothermic) and the requirements to produce steam in excess and condense the unreacted products are energetically unfavorable. Therefore, with low S/C ratios, the process needs a small amount of steam at the inlet and the excess is produced *in situ* by the electrochemical oxidation of the hydrogen obtained during the steam reforming reaction in the anode side;[81,82] this requires the development of specific materials.

During 8 h of reaction, CH_4 molar conversion was calculated (Figure 7 A) and the outlet gas compositions (H_2, CO, and CO_2) was analyzed (Figure 7 B). In those figures, two main zones are clearly evidenced with a first region in which a low conversion and low products composition are measured but gradually increase until they reach a second region of stable behavior. The latter, which corresponds to steady-state operation and starts after around 200 min, was used to determine the average values of conversion, gas compositions and selectivity, in a similar way as presented by other authors.[83]

10.1002/cctc.201901002

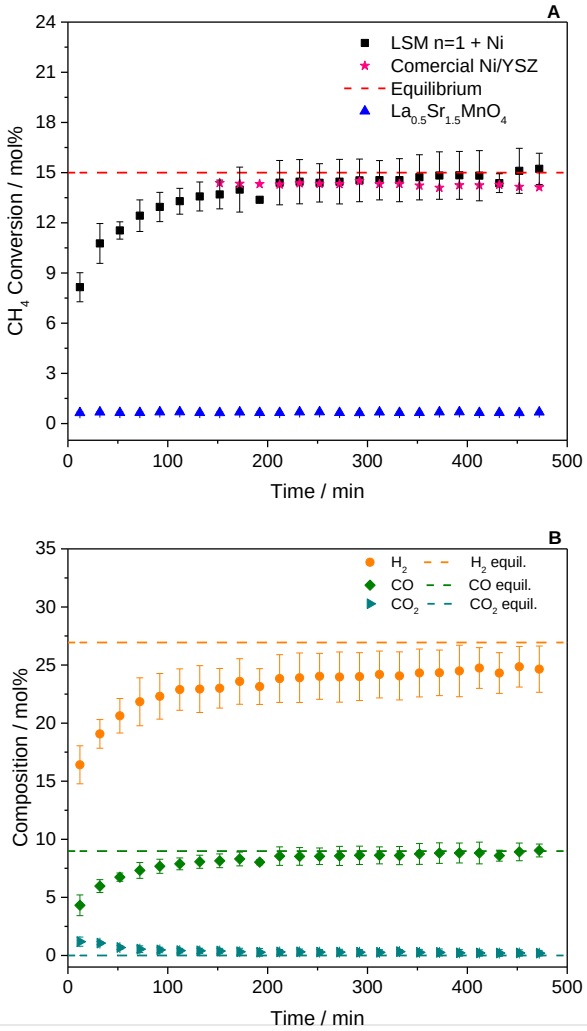

Figure 7. Catalytic behavior of LSMN n= 2 reduced at T=850 °C for 16 h A) CH_4 molar conversion at 850 °C (theoretical equilibrium as dashed line), compared with $La_{0.5}Sr_{1.5}MnO_4$ B) H_2, CO and CO_2 molar composition in comparison to theoretical equilibrium (dashed lines).

The direct influence of the Ni particles on the catalytic behavior is evident by the comparison with a pure LSM material (similar in composition to the support of the exsolved material), the latter having very poor catalytic activity. The resulting LSM n= 1 + Ni exhibits an exceptional activity: 24.19 mol% H_2, 0.26 mol % CO_2, 8.65 mol% CO corresponding to a stable CH_4 conversion (14.60 mol%). The obtained values are very close to the maximum CH_4 conversion, H_2, CO_2 and CO content that should be obtained with the selected operating conditions (equilibrium) or those obtained using Ni/YSZ material (Figure 7 A). The latter, comparable only from a purely catalytic behavior point of view and during few hours, because in previous works have been demonstrated that the major difficulty of a direct natural gas (methane) operation over Ni/YSZ is the possible formation/deposition of carbon species on the Ni surface due to cracking of hydrocarbons resulting in the loss of cell performance and low durability.[84–87]

Notwithstanding these results, it is not possible a complete and direct comparison between both materials reduced LSMN n= 2 and Ni/YSZ) because they are on the thermodynamic equilibrium. However, this preliminary result shows the high catalytic potential of the exsolved LSMN n= 2 for the steam reforming reaction in the selected operating conditions and therefore to be considered as anode materials for SOFC; in a forthcoming study, the influence of the exsolution conditions on the catalytic behavior and stability over longer times (coke formation/deposition) will be presented.

Table 3. Catalytic results of exsolved LSMN n = 2

H_2 formation rate [mol min^{-1} g^{-1}]	CH_4 conversion rate [mol min^{-1} g^{-1}]	S_{CO_2}	S_{CO}	H_2/CO ratio
$16.7x10^{-3}$ ± $1.45x10^{-3}$	$6.15x10^{-3}$ ± $0.42x10^{-3}$	0.03 ± $5x10^{-3}$	0.97 ± 5 $x10^{-3}$	2.80 ± 0.03

$$CO+H_2O \leftrightarrow CO_2+H_2 \quad \Delta H°=-41.2 \text{ kJ mol}^{-1} \qquad (5)$$

$$CH_4+H_2O \leftrightarrow CO+3H_2 \quad \Delta H°=206.1 \text{ kJ mol}^{-1} \qquad (6)$$

In addition, the presented results, together with the low CO_2 production (0.26 mol%) and the calculated H_2/CO ratio (2.80) measured in the effluent stream suggest a practically null contribution of Water-Gas Shift reaction [Eq. (5)][88] and the total selectivity towards the steam reforming reaction [Eq. (6)][88] using the exsolved material as catalyst (see Table 3). The catalytic behavior was maintained for more than 4 h, with a stable CH_4 conversion and H_2 formation rate, a much better behavior as other catalysts studied in similar S/C and temperature conditions, *e.g.* $Ce_{0.9}Gd_{0.1}O_{2-x}$ ($4.74x10^{-5}$ mol min^{-1} g^{-1})[89] or $Ir/Ce_{0.9}Gd_{0.1}O_{1.95}$ ($4.31 x10^{-4}$ mol min^{-1} g^{-1})[90] (Table 3). This apparent stability could be a sign of a potentially good resistance to coke formation/deposition in severe operating conditions (S/C= 0.15), which could be result of the fine metal dispersion and the strong basicity of the La/Sr-containing support grant less sensitivity to coking.[32,91]. Future studies with longer reaction time will be carried out to confirm such hypothesis.

Conclusions

In conclusion, the new material LSMN with n= 2 Ruddlesden-Popper structure was successfully synthesized by Pechini method as a single phase in air. In reducing atmosphere (H_2), at high temperature (750, 800 and 850°C) and different reduction times (4, 8 16, 24 and 48 h), an exsolution reaction occurs, resulting in the formation of LSM n= 1 together with embedded metallic Ni nanoparticles without any other impurity, as demonstrated by XRD analysis, TEM, and SEM, and with a direct influence on the particle size distributions and their average values. According to the preliminary test, and based on the catalytic behavior, the exsolved LSMN n= 2 material appears to be an interesting option to be considered as anode materials for SOFC fed with natural gas (methane) in low steam conditions, due to its high CH_4 conversion, H_2 production, selectivity to steam reforming reaction and a constant behavior once the steady state is reached. These catalytic properties could be an important proof to believe in the resistance of the new materials to coke

formation/deposition, but this is only a hypothesis for which a deeper and adequate study, is now required to support such conclusion.

Experimental Section

Synthesis

Powder of $La_{1.5}Sr_{1.5}Mn_{1.5}Ni_{0.5}O_{7\pm\delta}$ composition (hereafter referred to as LSMN n= 2) powder was synthesized by a Pechini o citrate complexation route[92] using stoichiometric amounts of La_2O_3 (≥ 99.9 % Alfa Aesar), $SrCO_3$ (≥ 99.9 % Sigma Aldrich), $MnCO_3$ (≥ 99.9 % Sigma Aldrich) and $NiCO_3$ (≥ 99.9 % Alfa Aesar). Before using La_2O_3 and $SrCO_3$, they were calcined in air at 1000 and 500 °C, respectively, for 1 hour. Such pre-treatments were performed to remove hydration products (and carbonation in the case of lanthanum oxide) in order to facilitate the weighing of the precursors in correct proportions. The precursors were initially dissolved in a solution made of concentrated nitric acid (HNO_3, ≥65 % Merck) in excess and citric acid (CA, ≥99.5 % Merck), added in the molar ratio $CA:(metal\ ion)_{total}$= 3:1. Under constant stirring, the resulting solution was slowly heated from room temperature to 120 °C using a hot plate, in order to reduce the volume of liquid. Polyethylene glycol (≥ 99 %, Panreac) was added as polymerizing agent (1.5 mL per gram of targeted product). Then, the resulting mixture was stirred and heated at 150 °C just to form a viscous gel, which was subsequently dried and heat-treated in air at 300 °C (2 h) and 500 °C (3 h) to ensure total organic matter decomposition. Finally, the product was subsequently sintered in air at 1000 °C (6 h), 1100 °C (6 h) and 1300 °C (12 h), with intermediate grinding and pelletizing steps. In order to assure a good homogeneity in the particle size of LSMN n= 2 material, the powder was ball-milled in an acetone:powder:3 mm-sized zirconia balls dispersion (5:1:5 weight ratio) during 12 h at a speed of 50 rpm. After milling step, the balls were separated, and the resulting mixture was dried. Homogenous powders with particle size distribution between 125 and 200 μm, were re-obtained by sieving through steel sieves of the referred mesh size.

Characterization

Each synthesized powder (~3 g per synthesis) was characterized by X-ray diffraction (XRD) at room temperature (RT) using a BrukerD8-ADVANCE powder diffractometer operated in Bragg-Brentano geometry, equipped with a Lineal LynxEye detector and a beam of CuKα1,2 radiation (λ= 1.5418 Å). The diffractometer was operated over the angular range 2θ= 2 - 70° for qualitative analysis and 2θ= 2 - 90° for Rietveld analysis with a measurement step of 0.020353° (2θ). The X-ray diffraction data were processed using JANA 2006 software package.[93] The elemental analysis was confirmed by X-Ray Fluorescence spectroscopy (XRF) in an S2 Ranger Bruker spectrometer equipped with a Pd X-ray tube.

Exsolution study

Thermogravimetric measurement in reducing atmosphere was carried out to understand the LSMN n= 2 reduction behavior in this atmosphere. The test was performed using a gravimetric analyser Hiden-Isochema model IGA-003, applying the first cycle in N_2 at 5 °C min^{-1} that aims to suppress any further influence of moisture and/or adsorbed species and then, then a second cycle one at 2 °C min^{-1} in 3 mol% H_2/N_2; both from RT to 1000 °C.

Reduction study: The operating temperatures (T) for the reduction study were selected considering the results obtained by TGA. Around 0.5 g of fresh LSMN n= 2 powder was reduced in a tubular furnace CARBOLITE CTF 12/65/550 using a gas mixture 3 mol% H_2/N_2 (Cryogas) with a flow of 55 mL (STP) min^{-1} and different reduction times (t_r= 1, 4, 8, 16, 24 and 48 h). The powder obtained at each temperature-reduction time point was characterized by XRD at RT as previously described. An additional microstructural characterization was performed on the reduced powder by field-emission scanning electron microscopy (FE-SEM) in a ZEISS microscope model ULTRA 55 and transmission electron microscopy in the TEM FEI TITAN Themis 300 equipped with a Super-X quad EDS for elemental analysis. The powder was crushed and dropped in the form of alcohol suspension on carbon supported copper grids followed by evaporation under ambient condition.

Catalytic test

Experimental set up: Steam reforming reaction with low steam content was studied on the LSMN n= 2 powder for selected reduction conditions to explore its potential as catalyst for this reaction. In further research this topic will be studied into details. The measurements of catalytic behavior for the reforming of methane were carried out in an experimental set-up. It is divided into 4 main sections: the first one is the gases zone in which N_2 (grade 5.0, CRYOGAS), 3 mol% H_2/N_2 mixture (Cryogas) and CH4 (grade 4.0, Cryogas) cylinders are available. In addition, this zone presents two analog manometers (Bourdon-Haenni® 0-100 psi and Ashcroft® 0-100 psi), two Cole-Parmer® 150 mm correlated and calibrated flowmeters with high-resolution valves and a Cole-Parmer® digital mass flowmeter (0-256 mL (STP) min^{-1}) for the precise control flow that passes to the next zones. The second zone is the gases saturation zone (humidification), which consists of a stainless-steel bubbler with a capacity of 300 mL, equipped with a type J immersion thermocouple and a clamp-on heater connected to its own control system. Additionally, a 50 cm heating cord, also with its own control system, wraps the bubbler outlet line to prevent the steam condensation before entering the reactor. The third zone is the reduction/reaction zone integrated by a tubular quartz reactor ($ø_I$: 9 mm, $ø_E$: 12 mm and L: 300 mm) heated by a tubular furnace (CARBOLITE MTF 10/15/130) and a cold trap to condense the steam excess after the reaction and before entering the gas chromatograph. According to the need (reduction step, reaction step or reagents analysis step) the bypass, line A or B will be used. Finally, the last zone is the analysis one, integrated by a gas chromatograph (GC, SRI instruments 8610C) using He (grade 5.0, CRYOGAS) as mobile phase, equipped with two packed columns (molecular sieve 13X 6 in and hayesep D 6 in), a thermal conductivity detector (TCD) and controlled by PeakSimple 4.44 free software.

Operating conditions: Around 100 mg of catalyst (LSMN n=2) was diluted in SiC (SiC:LSMN n= 2 10:1 weight ratio) and introduced in the reactor as fixed-bed between catalyst-free SiC and two pieces of quartz wool. Prior to the behavior test, the catalyst sample was reduced in situ (55 mL (STP) min^{-1} of 3 mol% H_2/N_2 mixture, Cryogas) according to the results obtained in the reduction study. The catalytic behavior was measured during 8 h at the same reducing temperature under atmospheric pressure. The reaction mixture corresponds to 82 mol% CH_4 (N_2 as balance) humidified in a steam to carbon ratio (S/C) of 0.15 according to the SOFC anode conditions suggested by the Gradual Internal Reforming concept or GIR.[81] The steam content was adjusted by flowing the adequate dry CH_4-N_2 mixture throughout the bubbler containing distilled water maintained exactly 46 °C. The total dry flow rate was 128 mL (STP) min^{-1} and the system was operating at a volume hourly space velocity (VHSV) of 86200 mL (STP) $min^{-1}\ g_{cat}^{-1}$. The composition in each effluent constituent (CH_4, CO, H_2, CO_2, and N_2) was obtained at regular time intervals (each 20 min) using online GC analysis. The CH_4 conversion (X_{CH_4}), CH_4 conversion rate and H_2 formation rate were calculated using Eq.(7), (8) and (9) respectively, where $n_{CH_4}^{In}$ and $n_{CH_4}^{Out}$ are the CH_4 molar flow rate at the inlet and outlet of the reactor (mol min^{-1}), W_{cat} is the catalyst weight (g), and $n_{H_2}^{Out}$ is the H_2 molar flow rate at the outlet of the reactor (mol min^{-1}). Blank tests were performed at different temperatures using SiC only, and no conversion was observed for methane.

$$X_{CH_4}=\frac{n_{CH_4}^{In}-n_{CH_4}^{Out}}{n_{CH_4}^{In}}\times 100 \quad mol\% \qquad (7)$$

$$CH_4\ conversion\ rate=\frac{n_{CH_4}^{In}-n_{CH_4}^{Out}}{W_{cat}} \quad mol\ min^{-1}g^{-1} \qquad (8)$$

$$H_2\ conversion\ rate=\frac{n_{H_2}^{Out}}{W_{cat}} \quad mol\ min^{-1}g^{-1} \qquad (9)$$

The CO and CO2 selectivities (S_{CO} and S_{CO_2}) were defined as the molar flow rate ratios of the specified component in the outlet (n_{CO} or n_{CO_2}) to the total produced CO and CO_2 molar flow rate ($n_{CO}+n_{CO_2}$) [Eq. (10) and (11)]. The H_2 to CO ratio is defined as is shown in Eq.(12).

$$S_{CO}=\frac{n_{CO}}{(n_{CO}+n_{CO_2})} \quad dimensionless \qquad (10)$$

$$S_{CO_2}=\frac{n_{CO_2}}{(n_{CO}+n_{CO_2})} \quad dimensionless \qquad (11)$$

$\frac{H_2}{CO} = \frac{n_{H_2}}{n_{CO}}$ dimensionless (12)

Acknowledgements

The authors acknowledge the financial support of the Colombian Administrative Department of Science, Technology and Innovation COLCIENCIAS (Project # 110265842833 "*Symmetrical high temperature Fuel Cell operating with Colombian natural gas*" (contract # 038-2015) and S. Vecino-Mantilla´s Ph.D. scholarship (call #647)) and of the Spanish National Research Council CSIC (Project # COOPA20112). The authors are also grateful to UIS' X-Ray Laboratory (Parque Tecnológico Guatiguará) for XRD measurements, UPV´s Electronic Microscopy Laboratory for the FESEM analysis, and finally to Margarita Vecino-Mantilla, Carolina Cárdenas-Velandia, Santiago Páez-Duque, Ivan Suárez-Acelas (UIS), María Fabuel (UPV) and Olivier Gardoll (UCCS) for their contribution to materials synthesis and characterization. As well as Santiago Palencia, Mónica Sandoval (UIS) and Caroline Pirovano (UCCS) are warmly acknowledged for useful discussions.

Keywords: Exsolution • Fuel cells • Nickel • Ruddlesden-Popper • Steam reforming

[1] S. P. S. Shaikh, A. Muchtar, M. R. Somalu, *Renew. Sustain. Energy Rev.* **2015**, *51*, 1–8.

[2] B. Shri Prakash, S. Senthil Kumar, S. T. Aruna, *Renew. Sustain. Energy Rev.* **2014**, *36*, 149–179.

[3] H. Ghezel-Ayagh, B. Borglum, *ECS Trans.* **2017**, *78*, 77–86.

[4] B. H. Park, G. M. Choi, *Solid State Ionics* **2014**, *262*, 345–348.

[5] Y. S. Chung, T. Kim, T. H. Shin, H. Yoon, S. Park, N. M. Sammes, W. B. Kim, J. S. Chung, *J. Mater. Chem. A* **2017**, *5*, 6437–6446.

[6] Y. Sun, J. Li, Y. Zeng, B. S. Amirkhiz, M. Wang, Y. Behnamian, J. Luo, *J. Mater. Chem. A* **2015**, *3*, 11048–11056.

[7] Y. Hu, Y. Bouffanais, L. Almar, A. Morata, A. Tarancon, G. Dezanneau, C. Paris, G. Voie, *Int. J. Hydrogen Energy* **2013**, *38*, 3064–3072.

[8] Y. Li, W. Zhang, Y. Zheng, J. Chen, B. Yu, Y. Chen, M. Liu, *Chem. Soc. Rev.* **2017**, *46*, 6345–6378.

[9] V. V. Kharton, A. A. Yaremchenko, A. L. Shaula, M. V. Patrakeev, E. N. Naumovich, D. I. Logvinovich, J. R. Frade, F. M. B. Marques, *J. Solid State Chem.* **2004**, *177*, 26–37.

[10] S. J. Skinner, J. A. Kilner, *Solid State Ionics* **2000**, *135*, 709–712.

[11] P. V. Balachandran, D. Puggioni, J. M. Rondinelli, *Inorg. Chem.* **2014**, *53*, 336–348.

[12] C. Autret, C. Martin, M. Hervieu, R. Retoux, B. Raveau, G. André, F. Bourée, *J. Solid State Chem.* **2004**, *177*, 2044–2052.

[13] J. Dailly, S. Fourcade, A. Largeteau, F. Mauvy, J. C. Grenier, M. Marrony, *Electrochim. Acta* **2010**, *55*, 5847–5853.

[14] H. Zhao, F. Mauvy, C. Lalanne, J. M. Bassat, S. Fourcade, J. C. Grenier, *Solid State Ionics* **2008**, *179*, 2000–2005.

[15] M. Al Daroukh, V. V. Vashook, H. Ullmann, F. Tietz, I. Arual Raj, *Solid State Ionics* **2003**, *158*, 141–150.

[16] S. Y. Jeon, M. B. Choi, H. N. Im, J. H. Hwang, S. J. Song, *J. Phys. Chem. Solids* **2012**, *73*, 656–660.

[17] H. W. Nie, T. L. Wen, S. R. Wang, Y. S. Wang, U. Guth, V. Vashook, *Solid State Ionics* **2006**, *177*, 1929–1932.

[18] Y. S. Yoo, M. Choi, J. H. Hwang, H. N. Im, B. Singh, S. J. Song, *Ceram. Int.* **2015**, *41*, 6448–6454.

[19] A. Das, E. Xhafa, E. Nikolla, *Catal. Today* **2016**, *277*, 214–226.

[20] S. Liping, H. Lihua, Z. Hui, L. Qiang, C. Pijolat, *J. Power Sources* **2008**, *179*, 96–100.

[21] C. Jin, Z. Yang, H. Zheng, C. Yang, F. Chen, *Electrochem. commun.* **2012**, *14*, 75–77.

[22] M. V. Sandoval, C. Pirovano, E. Capoen, R. Jooris, F. Porcher, P. Roussel, G. H. Gauthier, *Int. J. Hydrogen Energy* **2017**, *42*, 21930–21943.

[23] S. Li-Ping, L. Qiang, H. Li-Hua, Z. Hui, Z. Guo-Ying, L. NAN, J. P. Vircelle, C. Pijolat, *J. Power Sources* **2011**, *196*, 5835–5839.

[24] J. Shen, G. Yang, Z. Zhang, W. Zhou, W. Wang, Z. Shao, *J. Mater. Chem. A* **2016**, *4*, 10641–10649.

[25] L. Thommy, O. Joubert, J. Hamon, M. T. Caldes, *Int. J. Hydrogen Energy* **2016**, *41*, 14207–14216.

[26] J. T. S. Irvine, D. Neagu, M. C. Verbraeken, C. Chatzichristodoulou, C. Graves, M. B. Mogensen, *Nat. Energy* **2016**, *1*, 1–13.

[27] J. Zhou, T. H. Shin, C. Ni, G. Chen, K. Wu, Y. Cheng, J. T. S. Irvine, *Chem. Mater.* **2016**, *28*, 2981–2993.

[28] B. Hua, M. Li, Y. F. Sun, J. H. Li, J. L. Luo, *ChemSusChem* **2017**, *10*, 3333–3341.

[29] C. Yang, J. Li, Y. Lin, J. Liu, F. Chen, M. Liu, *Nano Energy* **2015**, *11*, 704–710.

[30] W. Zhang, W. Zheng, *ChemCatChem* **2015**, *7*, 48–50.

[31] S. Liu, W. Zhang, T. Deng, D. Wang, X. Wang, X. Zhang, C. Zhang, W. Zheng, *ChemCatChem* **2017**, *9*, 3102–3106.

[32] C. Arrivé, T. Delahaye, O. Joubert, G. Gauthier, *J. Power Sources* **2013**, *223*, 341–348.

[33] Y. Gao, D. Chen, M. Saccoccio, Z. Lu, F. Ciucci, *Nano Energy* **2016**, *27*, 499–508.

[34] Y. F. Sun, Y. Q. Zhang, J. Chen, J. H. Li, Y. T. Zhu, Y. M. Zeng, B. S. Amirkhiz, J. Li, B. Hua, J. L. Luo, *Nano Lett.* **2016**, *16*, 5303–5309.

[35] M. Henry, *Coord. Chem. Rev.* **1998**, *178–180*, 1109–1163.

[36] R. J. Ouellette, J. D. Rawn, *Org. Chem.* **2014**, 567–593.

[37] E. O. Chi, Y. U. Kwon, N. H. Hur, *Bull. Korean Chem. Soc.* **2000**, *21*, 259–263.

[38] A. A. Yaremchenko, D. O. Bannikov, A. V. Kovalevsky, V. A. Cherepanov, V. V. Kharton, *J. Solid State Chem.* **2008**, *181*, 3024–3032.

[39] T. I. Chupakhina, G. V. Bazuev, E. V. Zabolotskaya, *Russ. J. Inorg. Chem.* **2010**, *55*, 247–253.

[40] T. Jardiel, M. T. Caldes, F. Moser, J. Hamon, G. Gauthier, O. Joubert, *Solid State Ionics* **2010**, *181*, 894–901.

[41] K. Svoboda, A. Siewiorek, D. Baxter, J. Rogut, M. Pohořelý, *Energy Convers. Manag.* **2008**, *49*, 221–231.

[42] O. Kwon, S. Sengodan, K. Kim, G. Kim, H. Y. Jeong, J. Shin, Y. W. Ju, J. W. Han, G. Kim, *Nat. Commun.* **2017**, *8*, 1–7.

[43] J. Zhu, H. Li, L. Zhong, P. Xiao, X. Xu, X. Yang, Z. Zhao, J. Li, *ACS Catal.* **2014**, *4*, 2917–2940.

[44] I. K. Suh, H. Ohta, Y. Waseda, *J. Mater. Sci.* **1988**, *23*, 757–760.

[45] T. Broux, C. Prestipino, M. Bahout, O. Hernandez, D. Swain, S. Paofai, T. C. Hansen, C. Greaves, *Chem. Mater.* **2013**, *25*, 4053–4063.

[46] C. Munnings, S. Skinner, G. Amow, P. Whitfield, I. Davidson, *Solid State Ionics* **2006**, *177*, 1849–1853.

[47] R. K. Li, C. Greaves, *J. Solid State Chem.* **2000**, *153*, 34–40.

[48] Y. Wang, K. Shih, X. Jiang, *Ceram. Int.* **2012**, *38*, 1879–1886.

[49] D. Senff, P. Reutler, M. Braden, O. Friedt, D. Bruns, A. Cousson, F. Bourée, M. Merz, B. Büchner, A. Revcolevschi, *Phys. Rev. B - Condens. Matter Mater. Phys.* **2005**, *71*, 024425(1)-024425(8).

[50] S. Larochelle, A. Mehta, L. Lu, P. K. Mang, O. P. Vajk, N. Kaneko, J. W. Lynn, L. Zhou, M. Greven, *Phys. Rev. B* **2005**, *71*, 024435(1)-024435(18).

[51] M. Bieringer, J. E. Greedan, *J. Mater. Chem.* **2002**, *12*, 279–287.

[52] H. J. Kitchen, I. Saratovsky, M. A. Hayward, *Dalt. Trans.* **2010**, *39*, 6098–6105.

[53] J. Bandyopadhyay, K. P. Gupta, *Cryogenics (Guildf).* **1977**, *17*, 345–347.

[54] K. Y. Lai, A. Manthiram, *Chem. Mater.* **2018**, *30*, 2838–2847.

[55] G. Blasse, *J. Inorg. Nucl. Chem.* **1965**, *27*, 2683–2684.

[56] Y. Moritomo, Y. Tomioka, A. Asamitsu, Y. Tokura, *Phys. Rev. B* **1995**, *51*, 3297–3301.

[57] P. Ganguly, C. N. R. Rao, *J. Solid State Chem.* **1984**, *53*, 193–216.

[58] A. Benabad, A. Daoudi, *J. Solid State Chem.* **1977**, *22*, 121–126.

[59] W. B. Wu, D. J. Huang, G. Y. Guo, H. J. Lin, T. Y. Hou, C. F. Chang, C. T. Chen, A. Fujimori, T. Kimura, H. B. Huang, et al., *J. Electron Spectros. Relat. Phenomena* **2004**, *137–140*, 641–645.

[60] V. M. Gonzalez-DelaCruz, J. P. Holgado, R. Pereñíguez, A. Caballero, *J. Catal.* **2008**, *257*, 307–314.

[61] O. Dulub, W. Hebenstreit, U. Diebold, *Phys. Rev. Lett.* **2000**, *84*, 3646–3649.

[62] T. Wei, L. Jia, H. Zheng, B. Chi, J. Pu, J. Li, *Appl. Catal. A Gen.* **2018**, *564*, 199–207.

[63] A. Adamson, A. Gat, *Physical Chemistry of Surfaces*, John Wiley & Sons, Inc., New York, **1997**.

[64] T. S. Oh, E. K. Rahani, D. Neagu, J. T. S. Irvine, V. B. Shenoy, R. J. Gorte, J. M. Vohs, *J. Phys. Chem. Lett.* **2015**, *6*, 5106–5110.

[65] M. Blander, J. L. Katz, *AIChE J.* **1975**, *21*, 833–848.

[66] C. L. Kelchner, S. Plimpton, *Phys. Rev. B - Condens. Matter Mater. Phys.* **1998**, *58*, 11085–11088.

[67] D. Neagu, G. Tsekouras, D. N. Miller, H. Ménard, J. T. S. Irvine, *Nat. Chem.* **2013**, *5*, 916–923.

[68] O. G. Raabe, *J. Aerosol Sci.* **1971**, *2*, 289–303.

[69] B. R. Pauw, C. Kästner, A. F. Thünemann, *J. Appl. Crystallogr.* **2017**, *50*, 1280–1288.

[70] G. Bergeret, P. Gallezot, in *Handb. Heterog. Catal. Online* (Eds.: G. Ertl, H. Knözinger, F. Schüth, J. Weitkamp), Wiley-VCH Verlag GmbH & Co. KGaA, Online, **2008**, pp. 738–765.

[71] D. Neagu, T. S. Oh, D. N. Miller, H. Ménard, S. M. Bukhari, S. R. Gamble, R. J. Gorte, J. M. Vohs, J. T. S. Irvine, *Nat. Commun.* **2015**, *6*, 1–8.

[72] T. W. Hansen, A. T. Delariva, S. R. Challa, A. K. Datye, *Acc. Chem. Res.* **2013**, *46*, 1720–1730.

[73] J. Lif, M. Skoglundh, L. Löwendahl, *Appl. Catal. A Gen.* **2002**, *228*, 145–154.

[74] F. N. Agüero, A. M. Beltrán, M. A. Fernández, L. E. Cadús, *J. Solid State Chem.* **2019**, *273*, 75–80.

[75] R. T. K. Baker, *J. Catal.* **1982**, *78*, 473–476.

[76] S. E. Wanke, P. C. Flynn, *Catal. Rev. Sci. Eng.* **1975**, *12*, 93–135.

[77] G. Palasantzas, T. Vystavel, S. A. Koch, J. T. M. De Hosson, *J. Appl. Phys.* **2006**, *99*, 024307(1)-024307(5).

[78] M. A. Asoro, P. J. Ferreira, D. Kovar, *Acta Mater.* **2014**, *81*, 173–183.

[79] Z. Du, H. Zhao, S. Yi, Q. Xia, Y. Gong, Y. Zhang, X. Cheng, Y. Li, L. Gu, K. Świerczek, *ACS Nano* **2016**, *10*, 8660–8669.

[80] D. Papargyriou, J. T. S. Irvine, *Solid State Ionics* **2016**, *288*, 120–123.

[81] P. Vernoux, J. Guindet, M. Kleitz, *J. Electrochem. Soc.* **1998**, *145*, 3487–3492.

[82] K. Girona, S. Sailler, P. Gélin, N. Bailly, S. Georges, Y. Bultel, *Can. J. Chem. Eng.* **2015**, *93*, 285–296.

[83] W. K. B. W. Ramli, Exsolved Base Metal Catalyst Systems with Anchored Nanoparticles for Carbon Monoxide (CO) and Nitric Oxides (NOx) Oxidation, Newcastle University, **2017**.

[84] N. Laosiripojana, S. Assabumrungrat, *J. Power Sources* **2007**, *163*, 943–951.

[85] V. Sadykov, N. Mezentseva, G. Alikina, R. Bunina, V. Pelipenko, A. Lukashevich, S. Tikhov, V. Usoltsev, Z. Vostrikov, O. Bobrenok, et al., *Catal. Today* **2009**, *146*, 132–140.

[86] A. Atkinson, S. Barnett, R. J. Gorte, J. T. S. Irvine, A. J. McEvoy, M. Mogensen, S. C. Singhal, J. Vohs, *Nat. Mater.* **2004**, *3*, 17–27.

[87] A. . L. Dicks, *J. Power Sources* **1998**, *71*, 111–122.

[88] P. S. Roy, N. K. Park, K. Kim, *Int. J. Hydrogen Energy* **2014**, *39*, 4299–4310.

[89] G. Postole, F. Bosselet, G. Bergeret, S. Prakash, P. Gélin, *J. Catal.* **2014**, *316*, 149–163.

[90] S. K. Cheah, L. Massin, M. Aouine, M. C. Steil, J. Fouletier, P. Gélin, *Appl. Catal. B Environ.* **2018**, *234*, 279–289.

[91] C. H. Bartholomew, *Catal. Rev. Sci. Eng.* **1982**, *24*, 67–112.

[92] M. P. Pechini, *Method of Preparing Lead and Alkaline Earth Titanates and Niobates and Coating Method Using the Same to Form a Capacitor*, **1967**, US3330697A.

[93] V. Petrícek, M. Dušek, L. Palatinus, *Zeitschrift fur Krist.* **2014**, *229*, 345–352.

10.1002/cctc.201901002

WILEY-VCH

Entry for the Table of Contents (Please choose one layout)

Layout 1:

FULL PAPER

An original way to perform the exsolution of Ni nanoparticles on a ceramic support is explored for the development of SOFC anode material. At high temperature and reducing atmosphere, the n=2 Ruddlesden-Popper phase $La_{1.5}Sr_{1.5}Mn_{1.5}Ni_{0.5}O_7$ transforms into the n=1 $LaSrMnO_4$ with complete exsolution of Ni nanoparticles, converting the material into an interesting catalyst for the methane steam reforming reaction.

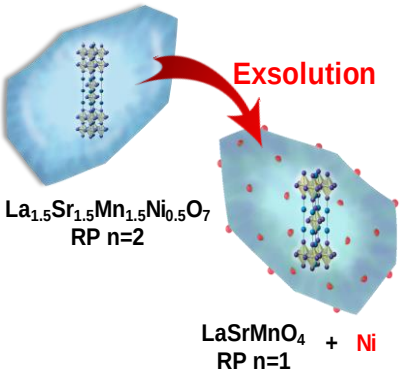

*S. Vecino-Mantilla, P. Gauthier-Maradei, M. Huvé J.M. Serra, P. Roussel, G. Gauthier**

Page No. – Page No.

Nickel exsolution-driven phase transformation from an n = 2 to an n= 1 Ruddlesden-Popper manganite for methane steam reforming reaction